Ultrafast Superconducting Single-Photon Optical Detectors and Their Applications

Introduction

Single-photon detectors (SPD's) represent the ultimate sensitivity limit for any quantum radiation detectors. In the visible light range, the best known and most widely used are Si avalanche photodiodes (APD's)[1] and photomultiplier tubes (PMT's).[2] The operation of photomultiplier/avalanche devices is based on the electron cascade and multiplication effect, which significantly amplifies the response and allows for an easy measurement of the response pulses. Unfortunately, this method of registration leads to a large time lag and jitter of the device response. In addition, the counting rates of APD's and PMT's are well below 100 MHz. Their actual speed is even more limited since, for noise reduction purposes, they have to be used in a time-gated mode, which reduces their counting rates to 10 MHz or below.

Detection of single-photon infrared (IR) radiation remains a major technological challenge because IR photons carry significantly less energy than those of visible light, making it difficult to engineer an efficient electron cascade. The most successful Si APD's have their sensitivity restricted by the band gap, while APD's based on narrow-gap semiconductors exhibit unacceptably large dark counts.[3] The best quantum efficiency (QE) reported for InGaAs APD's is ~16% at 1.2 μm, but the large, ~0.5-ns jitter and high, >10^4-per-second dark counts[3] make them unattractive for several important applications, including practical quantum communication systems.[2,4] The PMT's are bulky and demonstrate QE < 0.001% at 1.2 μm and ~150-ps jitter.[2] Finally, the most recently proposed far-IR detectors based on single-electron transistors[5] are very slow and require millikelvin temperatures.

In this article, we review our most recent research on superconducting SPD's (SSPD's). We demonstrate their excellent operating parameters and show that in many areas they drastically outperform their semiconductor counterparts. Applications ranging from visible free-space and IR fiber-based quantum communications[4] to nondestructive testing of very-large-scale-integrated (VLSI) devices[6] require SPD's with very high counting rates, very low jitter, and negligible dark counts. Effective operation in the mid-IR spectrum range is also very important. Our nanostructured, NbN SSPD's,[7,8] based on the nonequilibrium hot-electron effect in ultrathin superconducting films,[9] offer picosecond time resolution and jitter, experimental QE ranging from >10% for visible light to 5% to 3% in the 1.3-μm to 1.55-μm IR range, and very low dark counts.

The following sections will (1) present an overview of the physics of operation of SSPD's; (2) briefly discuss our fabrication methods; (3) present the experimental results and show the SSPD performance; (4) review already identified applications of SSPD's for VLSI chip testing and quantum cryptography; and (5) present our conclusions, including the direct comparison with other SPD's.

Physics of Operation of SSPD

Superconducting devices have already become practical as radiation sensors because of their quantum nature and low-noise cryogenic operation environment.[9] The superconducting energy gap 2Δ is typically two to three orders of magnitude lower than the gap in semiconductors; thus, individual optical photons are able to generate a large number of excited carriers when hitting a superconductor.[10] Measuring the resulting electrical pulse allows precise detection of the photon arrival. The efficient avalanche also results in an enhanced resolution of energy-resolving devices, such as superconducting tunnel junctions,[11] and extends the range of detectable energies well into the IR range for photodetectors. Finally, energy relaxation time constants of excited electrons in superconductors are in the picosecond range for both the low-temperature[12] and high-temperature[13] superconductors, ensuring the gigahertz repetition rates for superconducting photon counters.

Our SSPD consists of a superconducting stripe whose thickness is less than the electron thermalization length. The device is operated at a temperature far below the material's critical temperature T_c, in a regime where the bias current I is close to the critical value I_c. Absorption of a photon leads to

the formation of a hotspot region[14] where superconductivity is suppressed or even destroyed [Fig. 93.29(a)]. During the initial thermalization, the hotspot grows in size [Fig. 93.29(b)] as hot electrons diffuse out of the hotspot core. The supercurrent, which biases the device, is expelled from the resistive hotspot volume and is concentrated in the "sidewalks" near the edges of the film [Fig. 93.29(c)]. If the current density after this redistribution exceeds the critical value outside the hotspot, phase-slip centers are created in the sidewalks, the superconductivity is destroyed, and the resistive barrier is formed across the entire width of the device [Fig. 93.29(d)], which, in turn, gives rise to a voltage signal with the amplitude proportional to I. The hotspot growth is followed by its healing, due to the relaxation/cooling of excited electrons and their out-diffusion. Thus, after an ~30-ps-long quasiparticle relaxation time,[12] the hotspot collapses, superconductivity (zero voltage state) is restored, and the detector is ready to register another photon.

The SSPD operation principle outlined above depends directly on the superconductor characteristics, including 2Δ, diffusivity, electron–electron, and electron–phonon interaction times, as well as on the device geometry. Our material-of-choice is NbN, characterized by the picosecond quasiparticle relaxation; it is suitable for photon counting in the <0.4-μm- to 3.5-μm-wavelength range. Photons with a wavelength of 1 μm create in a 10-nm-thick NbN stripe a hotspot of ~20-nm diameter.[8] This means that the single-quantum mode of the SSPD operation requires that the width of our NbN superconductive stripe should be 200 nm or narrower.
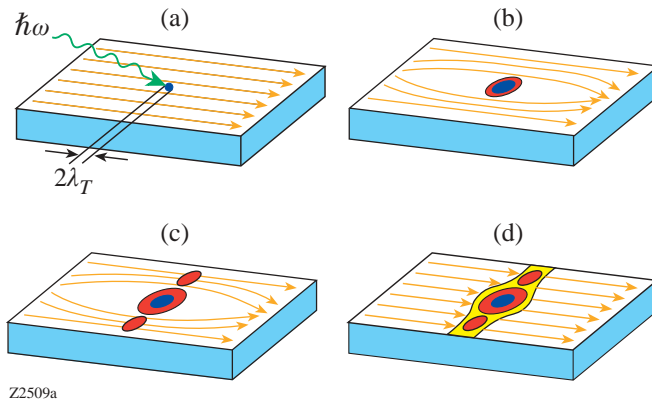
SSPD Fabrication

NbN superconductive films that we use to fabricate our SSPD's have a thickness of 3.5 nm to 10 nm and are deposited on sapphire substrates by dc reactive magnetron sputtering in an Ar and N$_2$ mixture.[15] The films are characterized by $T_c = 10$ to 11 K, the superconductive transition width $\Delta T_c \sim 0.3$ K, and the critical current density $j_c = 6$ to 7×10^6 A/cm^2 at 4.2 K. To implement a detector, we have chosen meander-type geometry with characteristic sizes ranging from 10×10 μm^2 to 4×4 μm^2 and a filling factor f (the ratio of the area occupied by the superconducting meander to the detector nominal area) up to 0.5. The width of the superconductive stripe varies from 80 nm to 200 nm. Our patterning and etching procedures are presented in detail in Ref. 15; here we mention only that our fabrication process includes an electron-beam lithography, followed by either ion milling through a Ti mask layer or reactive ion etching through a photoresist.

Figures 93.30 and 93.31 present scanning electron microscope images of two SSPD's that are fabricated according to two different patterning procedures described in Ref 15. Figure 93.30 shows a 10×8-μm^2, 10-nm-thick meander device, fabricated using the Ti mask and ion milling. We note that in this technology, although we can fabricate devices with very narrow (0.1 μm to 0.2 μm in width) meander stripes, f is always much lower than 1, as the separation between the lines remains significantly larger than the line width. Figure 93.31 presents the center part of our latest-generation, interdigitated structures with $f = 0.4$ to 0.5, etched in a 3.5-nm-thick NbN film. Using ultrathin films and direct reactive ion etching, we
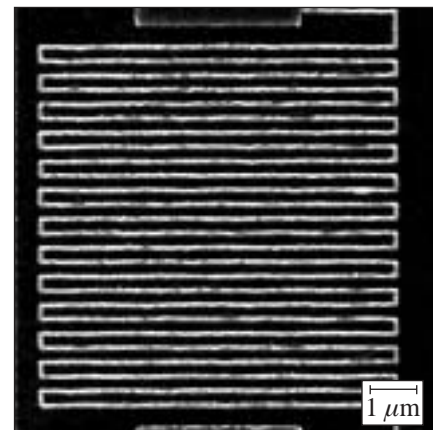

Z2509a

Figure 93.29
Schematics of the hotspot-generated and supercurrent-assisted formation of a resistive barrier in an ultrathin and submicrometer-width superconducting stripe, kept at a temperature far below T_c. The arrows indicate the flow direction of a supercurrent biasing the stripe.

Z2580

Figure 93.30
A scanning-electron-microscope image of a 10×8-μm^2, 10-nm-thick meander-type SSPD. The superconducting stripe width is ~130 nm and $f \approx 0.2$.
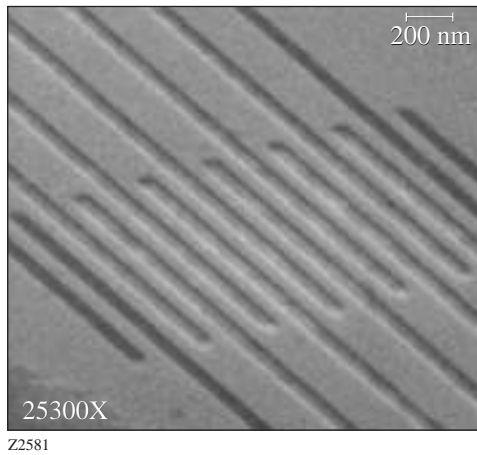
200 nm

25300X

Z2581

Figure 93.31
A scanning-electron-microscope image of an interdigitated, 3.5-nm-thick SSPD. The width of superconducting stripes (center of the picture) is ~80 nm and $f = 0.5$.
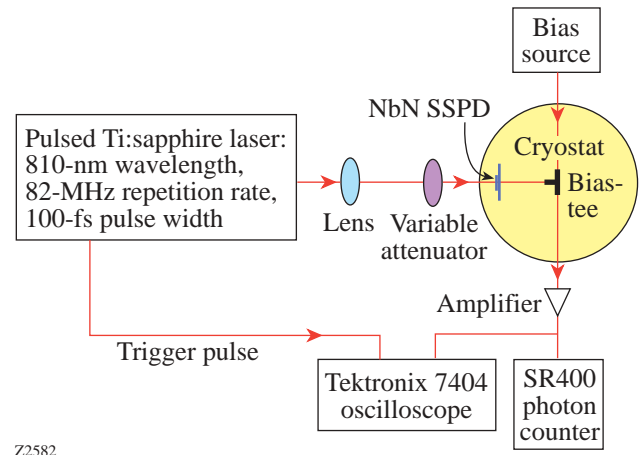

Z2582

Figure 93.32
Experimental setup for free-space detection of single photons.

not only increased f but also drastically reduced our SSPD stripe edge nonuniformities. This latter factor seems to be dominant in the device performance since, as will be presented later, the 3.5-nm-thick structures exhibited over-an-order-of-magnitude-higher experimental QE, despite having significantly decreased the photon absorption coefficient η.[7]

Experimental Results and the SSPD Performance

A schematic diagram of our experimental setup is shown in Fig. 93.32. The SSPD was placed on a cold plate inside an optical, liquid-helium cryostat and maintained at 4.2 K. The device was wire bonded to a microstrip transmission line and connected to the dc bias and rf output circuitry via a broadband, cryogenic bias-tee. The output signal, generated as a result of the photon capture, was amplified by a 20-dB-gain, room-temperature broadband amplifier and either fed into a Tektronix 7404 single-shot digital oscilloscope (synchronously triggered by a Ti:sapphire laser) or counted by an SR400 photon counter. The room-temperature amplifier and the oscilloscope were characterized by a bandwidth of 0.01 to 12 GHz and 0 to 4 GHz, respectively.

As a photon source, we used 100-fs-wide, 82-MHz-repetition-rate pulses from a self-mode-locked Ti:sapphire laser. The incident radiation was focused on the device and attenuated to the picowatt level, using banks of neutral-density filters. The optical beam diameter was typically ~50 μm to ensure the SSPD uniform illumination. In addition, the QE spectral sen-

sitivity dependence of the SSPD was measured using a continuous-wave (cw) blackbody radiation source and cw and pulsed laser diodes.

Figure 93.33 shows a collection of real-time "snapshots" recorded by the single-shot oscilloscope for different numbers of photons per laser pulse, incident on a 4×4-μm^2-area, 10-nm-thick SSPD, and is intended to illustrate the physical response of our devices. Each snapshot presents a 50-ns-long record of the response to four successive 100-fs-wide optical pulses, randomly selected out of a real-time detector output data stream. Trace (a) in Fig. 93.33 corresponds to essentially a macroscopic signal with ~20,000 photons per pulse hitting the detector. In this case, the device responded to each optical pulse in the laser train; however, as the incident laser intensity was decreased (with other experimental conditions unchanged), the quantum nature of the detector response started to emerge. For ~2400 photons per pulse [traces (b) and (c)], the amplitude of the response pulses was decreased, but, most interestingly, some of the signals were absent in the response train [trace (c)]. Further, over-an-order-of-magnitude decrease in the photon flux did not lead to the decrease of the output signal amplitude, which is characteristic of classical intensity detectors, but many of the response pulses were missing [trace (d)] due to both the limited QE of the device and fluctuations in the number of photons incident on the detector. The quantum nature of our device response was most apparent in the bottom pair of traces: (e) and (f) (1 photon/pulse). We note that
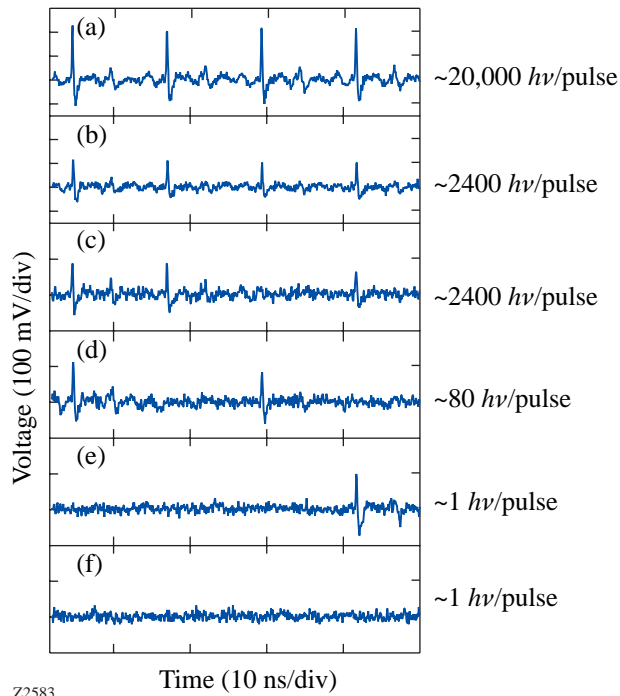
Z2583

Real-time responses of a SSPD to trains of 100-fs optical pulses with different numbers of photons per pulse per device area. The presented records illustrate the quantum nature of our device responses at low photon fluxes. Radiation wavelength was 810 nm.

Z2584

Figure 93.34
Probability of photon counting versus the incident photon radiation flux for a 10×10-μm^2, 10-nm-thick SSPD at 405-nm (squares), 810-nm (circles), and 1550-nm (triangles) wavelengths. The bias current was $I/I_c = 0.8$ and temperature was 4.2 K. The solid lines illustrate the slope exponents $n = 1$ and $n = 2$.

in each case, the detector response is very different and its actual performance has to be judged, based on the response averaged over the recording time much longer than 50 ns. We also note that within the time resolution of our electronics, the width of the SSPD response pulses remained constant for all tested photon fluxes.

Records like the ones shown in Fig. 93.33, but averaged over almost 5×10^9 optical pulses (accumulated over a period of 60 s using the SR400 counter), allowed us to perform statistical analysis of the SSPD response. We observed that for weak photon fluxes (<100 photons per pulse), both the average number of captured pulses for a given photon flux and the signal amplitude remained constant. Figure 93.34 shows the probability of photon counting (the ratio of the average number of photons captured per second to the repetition rate of laser pulses) as a function of the average number per pulse of 405-nm, 810-nm, and 1550-nm photons from our Ti: sapphire laser, incident on a 10×10-μm^2-area, 10-nm-thick device. The device was biased at $I = 0.8\ I_c$, which was low enough to remain subcritical even when I_c was thermally suppressed at the highest incident light intensities. We note
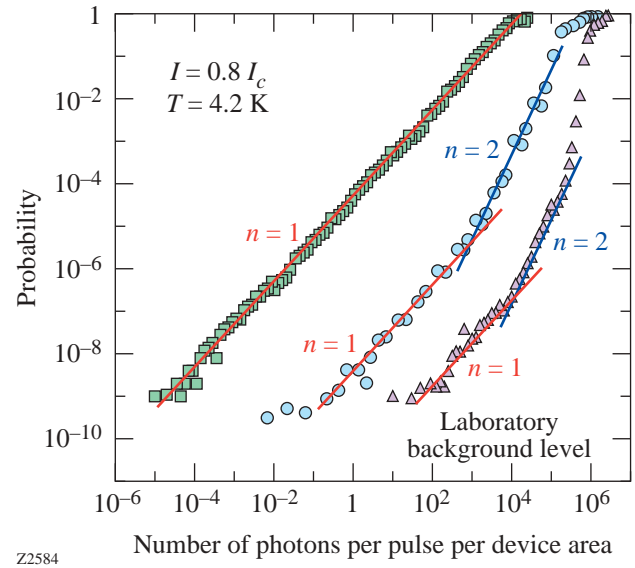
that for 405-nm photons we have a linear dependence over ten orders of magnitude of the photon flux intensity. At wavelength $\lambda = 810$ nm, we observe the linear response at low photon counts and the quadratic law for higher photon fluxes. Finally, for $\lambda = 1550$ nm, the photon counting rate is a highly nonlinear function of the photon flux, with the linear dependence observed only in the range of 10^2 to 10^4 photons per pulse. We also observe that for the lowest photon fluxes, our experimental data points, for every wavelength, level off at the same ~10^{-9} probability value (~0.1 counts per second). We interpret this response as the laboratory photon background, resulting from accidental photon absorption by our detector. On the other hand, the saturation (probability approaching 1) observed at the highest incident photon flux levels represents the transition of our quantum device into a classical detector [see also Fig. 93.33(a)].

SSPD's are passive devices, and the main sources of dark or false counts are either extrinsic bias-current instabilities or intrinsic fluctuations. The supercurrent fluctuations are dominating at I very close to I_c and rapidly (exponentially) decrease with the I decrease,[16] while thermally activated phase-slip centers are typically negligible since we operate our devices at $T \ll T_c$. Thus, long-term stability of I when the detector is biased close to I_c is crucial for minimizing dark counts. One

must remember, however, that SSPD's are very broadband sensors and they have to be properly screened from unwanted "photon noise." Large values of dark counts were observed in SSPD implementations, where thermal background radiation from room-temperature objects was inadvertently coupled into the detector.[6] Measurements of dark counts performed in the setup shown in Fig. 93.32 with the SSPD blocked by a cold load lead to an average of <0.01 counts per second for $I \leq 0.95 I_c$ and were, apparently, limited by our biasing electronics.

The behavior observed in Fig. 93.34 results from the direct linear dependence of the hotspot size on the photon energy.[8] Thus, for a fixed I, low-energy photons generate hotspots too small to ensure efficient SSPD operation, leading to enhanced probability of multiphoton detection with the increase of the photon flux.

For a mean number of m photons per pulse, the probability $P(n)$ of absorbing n photons from a given pulse is given by the Poisson distribution:

$$P(n) \sim \frac{e^{-m}(m)^n}{n!}. \tag{1}$$

For very weak ($m \ll 1$) photon fluxes, the probability of detecting one photon, two photons, three photons, etc., is

$$P(1) \sim m, \ P(2) \sim \frac{m^2}{2}, \ P(3) \sim \frac{m^3}{6}, \ \text{etc.} \tag{2}$$

Based on Eq. (2), we can conclude that for a very low number of photons per pulse incident on the SSPD, we clearly observe in Fig. 93.34 a single-photon detection regime (exponent $n = 1$) for each studied wavelength. While for 405-nm radiation, the presence of at least one photon in the optical pulse was sufficient to trigger the detector response, for $\lambda = 1550$ nm, the multiphoton absorption ($n \geq 2$) was dominant.

The probability of photon counting measured at the one-photon-per-pulse level incident upon the SSPD and expressed in percent can be defined as its *experimental* QE [more rigorously: detection efficiency (DE)] for a given photon energy. We must stress that QE is a function of I and the highest values are measured for I very close to I_c as shown in Refs. 8 and 16. Typically, we operate our SSPD's with $I \leq 0.95 I_c$ since, as we mentioned before, higher I values result in excessive dark counts. Figure 93.35 presents experimental QE spectral de-
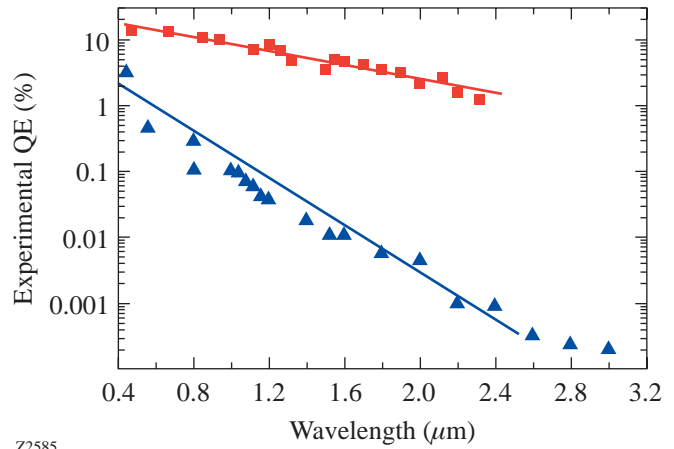

Figure 93.35
Spectral dependences of QE for 10×10-μm^2 SSPD's, with NbN stripe thickness of 10 nm (triangles) and 3.5 nm (squares), respectively. The solid lines are guides to the eye, illustrating the exponential dependence of the QE on wavelength.

pendence for two representative 10×10-μm^2-area devices. The 3.5-nm-thick SSPD (squares) was an interdigitated device (see Fig. 93.31) with 80-nm-wide NbN fingers and $f = 0.5$, while the 10-nm-thick, 200-nm-wide-stripe SSPD (triangles) was a meander-type structure (see Fig. 93.30) with $f \approx 0.2$. We observe that in both cases, the DE spectral dependence exhibited an exponential, activated-type character with the slope value characteristic for all devices with the same thickness.[8] We associate the activation-type behavior with the presence of fluctuations, both extrinsic (stripe width) and intrinsic (superconducting). Simultaneously, we note the drastic improvement in the performance of the 3.5-nm-thick device, as compared to the 10-nm structure, in terms of both the much smaller slope value and the much higher experimental QE.[16]

As we mentioned in the **SSPD Fabrication** section, this performance improvement is the result of significant improvements in our fabrication technology.[15] The interdigitated devices implement the ultrathin NbN stripe (larger hotspot dimension) and are truly nanostructured in terms of their physical dimensions. Our best 10-nm-thick SSPD's exhibit experimental QE of ~3% at $\lambda = 405$ nm, decreasing to ~0.01% at $\lambda = 1550$-nm wavelength. At the same time, the 3.5-nm devices reach over-an-order-of-magnitude-higher QE, ranging from >10% at $\lambda = 405$ nm to 3.5% at $\lambda = 1550$ nm.

Proper coupling of our devices to the incident photon flux is another, besides I, limiting factor of the SSPD's experimental QE value. Unlike semiconductor SPD's, the SSPD's have a

relatively small active area, and only a certain percentage of incident photons is actually absorbed in the ultrathin NbN stripe. The above limitations are extrinsic; thus, in order to estimate the SSPD ultimate performance, defined as the *intrinsic* QE of the superconducting stripe,[7,8] one needs to factor in both the filling factor and the photon absorption coefficient. For 10-nm-thick devices, $f \approx 0.2$ and $\eta \approx 0.3$, leading to the intrinsic QE = DE/$(f\eta)$, indicating that the possible improvement can reach up to a factor of 20. In the case of the 3.5-nm SSPD's, similar calculations indicate that the intrinsic QE should reach the theoretical maximum of 100% for all visible-light wavelengths. The above approach is questionable, however, since for our ultrathin, nanostructured devices, the NbN optical conductivity can be quite different from the dc value used in Eq. (1) in Ref. 7 to calculate η. The best approach to further increase the QE of our detectors is, we believe, not by changing the interdigitated SSPD geometry, but by adding a backside mirror to reflect the transmitted photons back into the detector. It would be even more effective to form a $\lambda/4$ resonator with the detector acting as one of the resonator mirrors. In this case, however, the SSPD would loose its broadband sensitivity.

Finally, one can define a *system* QE as the number of photons falling at input on the fiber or other coupling optics, divided by the number of photon counts recorded by the detector. This QE definition includes the impact of the detector coupling optics rather than the SSPD size, and it was used in Ref. 6 to describe the performance of the early SSPD-based system designed for noninvasive testing of the VLSI chips. The system QE value reported in Ref. 6 for one of the first 10-nm-thick, meander-type SSPD's was 0.002% at 1.3-μm wavelength. The latest 3.5-nm devices in the same fiber-based system (although with significantly modified/improved optics) exhibit a system QE of 2% at the same wavelength—a four-orders-of-magnitude improvement over a two-year period.

We have also performed extensive time-domain characterization of our SSPD's, which are presented in Ref. 17. Here we want only to mention that the 10-nm-thick SSPD's have a time resolution <100 ps and a device jitter <35 ps. Thus, they are able to detect photons with at least 10-Gbit/s counting rate and are more than three orders of magnitude faster than any semiconductor SPD. The 3.5-nm devices are expected to have even better time resolution, reaching values close to the intrinsic electron–phonon cooling time in ultrathin NbN films of 30 ps.[12] Their jitter has been already measured and is below 20 ps.

Applications of SSPD's
1. Noncontact VLSI Chip Testing

Modern, high-performance, electronic VLSI circuits are extremely difficult to test on both the functional and logic levels because of their complexity, density of packaging, and the use of flip-chip bonding. Devices are increasingly more sensitive and can be easily perturbed during testing, skewing results and slowing the design and development time. Thus, in complex circuits such as microprocessors, nonperturbing methods of testing the chip functionality while it operates are most desirable.

A normally operating silicon complementary metal oxide semiconductor (CMOS) transistor has a nonzero probability of emitting near-IR (0.9 μm to 1.4 μm) photons when current passes through the channel. This is the spontaneous photon emission associated with intraband transitions as the hot carriers move across the transistor channel.[18,19] Thus, this photon emission is time-correlated with the transistor switching event and measures directly the transistor switching time, as well as the entire circuit timing characteristics. This intrinsic transistor/circuit information is ideal for timing data acquisition and fault analysis (e.g., leaky transistors tend to emit more photons). The use of near-IR emission from CMOS integrated circuits as a way of diagnosing timing and flaws of VLSI chips has been implemented in the IDS PICA probe system, manufactured by NPTest, San Jose, CA. The IDS PICA system can be equipped with an imaging near-IR detector, the Mepsicron II PMT (Quantar Tech., Inc) or with the SSPD device.[6] The imaging PMT camera enables light emission from many devices on a test circuit to be simultaneously analyzed, but its IR efficiency is extremely low, leading to hour-long acquisition times and poor noise-to-signal ratio. The SSPD can analyze emission from a single CMOS device only, but its superior IR QE cuts acquisition times to minutes or seconds.

The 3.5-nm-thick NbN SSPD sensors are currently being implemented in the latest IDS PICA version. Test results from a 0.18-μm-linewidth, 1.6-V-bias CMOS integrated circuit running at 100 MHz are shown in Fig. 93.36. The collected histogram has an extremely high signal-to-noise ratio and the time between transistor switching events can be measured with 10-ps accuracy. In addition to the peaks coming from photon emission from nMOS transistors, we can also observe weak signals collected from pMOS inverters. Holes in pMOS devices have lower mobility and emit IR photons much less frequently. We need to stress that the integrated circuit under test and the photon-collecting microscope are at room tem-
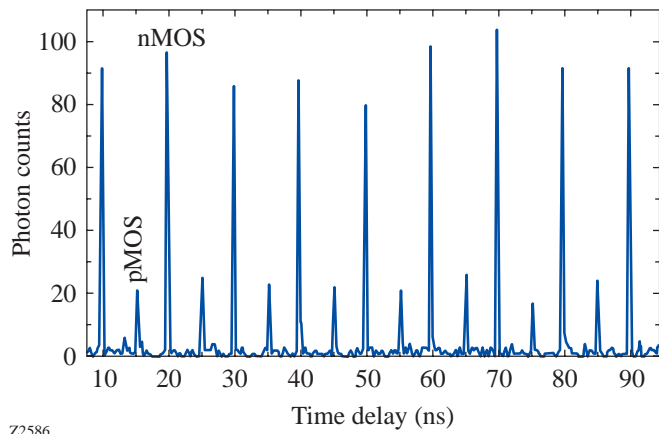
Figure 93.36
Histogram of single-photon emissions from a CMOS VLSI chip, collected by the NbN SSPD. Signals from both nMOS and pMOS transistors are clearly visible. The picture was copied directly from the PICA screen.

perature, and the microscope is connected to the SSPD via a multimode fiber. Physically, the chip-testing apparatus is approximately 2 to 3 m away from the detector, which is placed inside a commercial cryocooler, operating at 3.5 K.
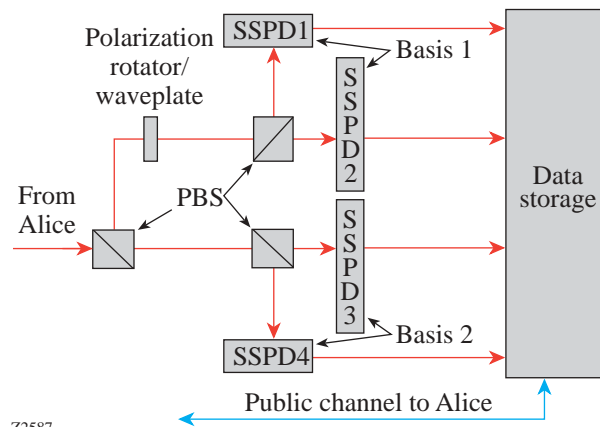
2. Quantum Cryptography

Quantum cryptography (QC) provides a radical improvement over today's methods for secure communications. Unconditionally secret communication is possible in actual physical environments due to the Heisenberg indeterminacy principle: it is impossible to measure the state of a quantum bit without altering it. In QC, the data transport is performed as an exchange of individual photons with their polarization used to code the logic information for the communication protocol. QC is based on the real-time Vernam encryption scheme (so-called "one-time pad").[20] The quantum key is formed during the photon transmission (there is no pre-existing key), and the Vernam cipher is invulnerable to any computer attack of any strength, including quantum computations.

A recent theoretical paper by Gilbert and Hamrick[21] proves that QC is practical, providing that the data transmission rate is high enough to overcome the intrinsic system losses. Both the transceiver (Alice) and the receiver (Bob) must operate at transmission rates of at least 1 Gbit/s for the practical quantum key distribution operation. A GHz-repetition-rate, actively mode-locked laser can be used as the high-speed source of coherent single photons,[22] so Alice can readily operate at the GHz range. A serious problem, however, exists at the Bob end,

which should count photons not only very efficiently, but also with negligible dark counts and very low jitter.

Figure 93.37 presents a possible QC receiver, containing four SSPD's for independent counting of photons with four different polarizations imprinted by Alice. The NbN SSPD's are the most promising for practical QC since, as we have already presented, they exhibit sufficiently high QE and are able to reach GHz-range counting rates with very low jitter and negligibly low dark counts. The SSPD's can successfully operate from ultraviolet to IR; thus, they can be implemented in both optical free-space and fiber-based transmission schemes.

Figure 93.37
Quantum cryptography receiver (Bob) based on four NbN SSPD's. PBS stands for polarization beamsplitter.

Conclusions

Table 93.II presents the main characteristics of our SSPD's, in direct comparison with other modern single-photon detectors. Experimental QE, ultimate counting rate, jitter, and dark counting rates are compared for 1.3-μm photons, which is the most-interesting wavelength for applications ranging from noninvasive VLSI chip testing to fiber-based optical communications. As can be seen, superconducting detectors significantly outperform even the best semiconductor devices.

Table 93.II: Performance of different SPD's operating at $\lambda = 1.3$ μm.

Detector Model	Counting Rate	QE	Jitter	Dark Counts
	(Hz)	(%)	(ps)	(s^{-1})
InGaAs APD (Fujitsu)	5.0×10^{6} [a]	16	200	500 [b]
IR PMT (Hammamatsu)	9.0×10^{6}	0.5	150	2.0×10^{4}
Si APD (EG&G)	5.0×10^{6}	0.01	350	25
Mepsicron (Quantar, Inc.)	1.0×10^{6} [c]	0.001	100	0.1
Superconducting tunnel junction	5.0×10^{3}	60	N/A	N/A
SSPD (measured)	10×10^{9}	5	35	0.1 [d]
SSPD (projected)	30×10^{9}	>10	<20	<0.01

[a]Gated regime with 0.1%-per-gate after-count probability.
[b]Calculated with 10^{-4}-per-gate probability.
[c]Data for a high-speed version; standard devices exhibit 1×10^{5} s^{-1}.
[d]Room-temperature input.

REFERENCES

1. T. Isoshima *et al.*, Rev. Sci. Instrum. **66**, 2922 (1995).

2. A. Karlsson *et al.*, IEEE Circuits and Devices Mag. **15**, 34 (1999).

3. F. Zappa *et al.*, Opt. Eng. **35**, 938 (1996).

4. A. A. Verevkin, J. Zhang, W. Slysz, R. Sobolewski, A. P. Lipatov, O. Okunev, G. Chulkova, A. Korneev, and G. N. Gol'tsman, in *Free-Space Laser Communication and Laser Imaging II*, edited by J. C. Ricklin and D. G. Voelz (SPIE, Bellingham, WA, 2002), Vol. 4821, pp. 447–454.

5. O. Astafiev *et al.*, Appl. Phys. Lett. **80**, 4250 (2002).

6. S. Somani, S. Kasapi, K. Wilsher, W. Lo, R. Sobolewski, and G. Gol'tsman, J. Vac. Sci. Technol. B, Microelectron. Nanometer Struct. **19**, 2766 (2001).

7. G. N. Gol'tsman, O. Okunev, G. Chulkova, A. Lipatov, A. Semenov, K. Smirnov, B. Voronov, A. Dzardanov, C. Williams, and R. Sobolewski, Appl. Phys. Lett. **79**, 705 (2001).

8. A. Verevkin, J. Zhang, R. Sobolewski, A. Lipatov, O. Okunev, G. Chulkova, A. Korneev, K. Smirnov, G. N. Gol'tsman, and A. Semenov, Appl. Phys. Lett. **80**, 4687 (2002).

9. A. D. Semenov, G. N. Gol'tsman, and R. Sobolewski, Supercond. Sci. Technol. **15**, R1 (2002).

10. K. S. Il'in, I. I. Milostnaya, A. A. Verevkin, G. N. Gol'tsman, E. M. Gershenzon, and R. Sobolewski, Appl. Phys. Lett. **73**, 3938 (1998).

11. A. Peacock *et al.*, Nature **381**, 135 (1996); R. J. Schoelkopf *et al.*, IEEE Trans. Appl. Supercond. **9**, 2935 (1999).

12. K. S. Il'in, M. Lindgren, M. Currie, A. D. Semenov, G. N. Gol'tsman, R. Sobolewski, S. I. Cherednichenko, and E. M. Gershenzon, Appl. Phys. Lett. **76**, 2752 (2000).

13. M. Lindgren, M. Currie, C. Williams, T. Y. Hsiang, P. M. Fauchet, R. Sobolewski, S. H. Moffat, R. A. Hughes, J. S. Preston, and F. A. Hegmann, Appl. Phys. Lett. **74**, 853 (1999).

14. A. M. Kadin and M. W. Johnson, Appl. Phys. Lett. **69**, 3938 (1996).

15. G. N. Gol'tsman, K. Smirnov, P. Kouminov, B. Voronov, N. Kaurova, V. Drakinsky, J. Zhang, A. Verevkin, and R. Sobolewski, "Fabrication of Nanostructured Superconducting Single-Photon Detectors," to be published in IEEE Transactions on Applied Superconductivity.

16. A. Lipatov, O. Okunev, K. Smirnov, G. Chulkova, A. Korneev, P. Kouminov, G. Gol'tsman, J. Zhang, W. Slysz, A. Verevkin, and R. Sobolewski, Supercond. Sci. Technol. **15**, 1689 (2002).

17. J. Zhang, W. Slysz, A. Verevkin, G. Chulkova, A. Korneev, A. Lipatov, O. Okunev, G. Gol'tsman, and R. Sobolewski, "Response Time Characterization of NbN Superconducting Single-Photon Detectors," to be published in IEEE Transactions on Applied Superconductivity.

18. J. C. Tsang and J. A. Kash, Appl. Phys. Lett. **70**, 889 (1997).

19. M. Pavesi *et al.*, Phys. Rev. B **65**, 195209 (2002).

20. G. S. Vernam, J. Amer. Inst. Elec. Eng. **XLV**, 109 (1926).

21. G. Gilbert and M. Hamrick, "Practical Quantum Cryptography: A Comprehensive Analysis (Part One)," MITRE Technical Report MTR00W0000052 (September 2000), http://xxx.lanl.gov/abs/quant-ph/0009027; also to be published in Physics Reports.

22. T. R. Clark *et al.*, Electron. Lett. **35**, 720 (1999).